Influence of Real Gas Properties on Aerodynamic Losses in a Supercritical CO_2 Centrifugal Compressor

YANG Mingyang[1*], CAI Ruikai[1], ZHUGE Weilin[2*], YANG Bijie[3], ZHANG Yangjun[2]

1. School of Mechanical Engineering, Shanghai Jiao Tong University, Shanghai 200240, China
2. School of Vehicle and Mobility, State Key Laboratory of Intelligent Green Vehicle and Mobility, Tsinghua University, Beijing 100084, China
3. Department of Mechanical Engineering, Imperial College London, London SW7 2AZ, UK

Abstract: Supercritical carbon dioxide (SCO_2) centrifugal compressor is a key component of a closed Brayton cycle system based on SCO_2. A comprehensive understanding of the loss mechanism within the compressor is vital for its optimized design. However, the physical properties of SCO_2 are highly nonlinear near the critical point, and the internal flow of the compressor is closely related to its properties, which inevitably influences the generation of aerodynamic losses within the compressor. This paper presents a comprehensive investigation of the compressor's loss mechanism with an experimentally validated numerical method. The real gas model of CO_2 embodied in the Reynolds-Averaged Navier-Stokes (RANS) model was used for the study. Firstly, the numerical simulation method was validated against the experimental results of Sandia SCO_2 compressor. Secondly, performance and loss distribution of the compressor were compared among three fluids including SCO_2, ideal CO_2 (ICO_2) and ideal air (IAir). The results showed that the performance of SCO_2 was comparable to IAir under low flow coefficient, however markedly inferior to the other two fluids at near choke condition. Loss distribution among the three fluids was distinctive. In the impeller, SCO_2 was the most inefficient, followed by ICO_2 and IAir. The discrepancies were magnified as the flow coefficient increased. This is due to a stronger Blade-to-Blade pressure gradient that intensifies boundary layer accumulation on walls of the shroud/hub. Furthermore, owing to the reduced sonic speed of SCO_2, a shock wave appears earlier at the throat region and SCO_2 encounters more intense boundary layer separation.

1. Introduction

Closed Brayton cycle based on SCO_2 inherently exhibits a range of advantages, notably in terms of cycle efficiency and compactness, which make them attractive for applications such as concentrate solar energy capture, direct-firing power plants, and industrial waste heat recovery [1–4]. Studies have revealed that for mid-temperature heat sources, such cycle exhibits an up to 5% efficiency improvement when compared with conventional steam Rankine cycles [5]. In such a cycle, the fluid is above the supercritical point (304 K, 7.31 MPa)

Nomenclature

Symbols			s	Isentropic
C_f	Skin friction coefficient		t	Total
d	Diameter		vis	Viscous
h	Enthalpy		0	Stagnation
k	Thermal conductivity		1	Inlet
P	Pressure		2	Exit
Q	Mass flow rate		**Abbreviations**	
Re	Reynolds number		CFD	Computational fluid dynamics
ΔS	Entropy generation		DNS	Direct numerical simulation
T	Temperature		EOS	Equation of state
V	Velocity		IAir	Ideal air
V_n	Dimensionless velocity		ICO_2	Ideal carbon dioxide
y^+	Normalized wall distance		LE	Leading edge
η	Efficiency		OP	Operational point
ρ	Density		PR	Normalized pressure ratio
σ	Entropy rise coefficient		PS	Pressure surface
Φ	Dissipation		RANS	Reynolds-Averaged Navier-Stokes
Subscripts			RGP	Real gas properties
ave	Mass-flow-rate average		SCO_2	Supercritical carbon dioxide
i, j	All dimension		SS	Suction surface

and the properties vary nonlinearly with temperature and pressure [6–8]. At temperatures approaching the critical point, a 1 K increase leads to approximate 10% and 6% increases in density and sonic speed respectively. The real gas properties inevitably affect the flow field, thus influencing the performance of the compressor. The common approach for a SCO_2 compressor design usually begins with a rough evaluation of performance via a meanline model. The optimization of the compressor relies heavily on the accuracy of such model. However, it is questionable how reliable a conventional method of performance prediction by the meanline model is.

Many researches have been conducted to investigate the influence of real gas properties of SCO_2 on the performance of a centrifugal compressor. Baltadjiev was the first to investigate the discrepancies of compressor performance with different working fluids via 2D numerical method [9]. The studies indicated that the centrifugal compressor (simplified into 2D geometries) using SCO_2 shows an efficiency about 1.1% higher than that using air with a comparable Machine Mach number. As the authors pointed out, due to the use of simplified 2D geometries which solely consider profile loss, the real gas properties did not exert a significant influence. Seong studied the reliability of a conventional 3D numerical method to predict the performance of a SCO_2 centrifugal compressor under varied inlet conditions [10]. Analysis of prediction and experimental results revealed that near

the critical point, their efficiency discrepancy is as much as 21%. Some recent researches focus on the effect of inlet condition near critical region to the SCO_2 centrifugal compressor performance [11–13]. The results pointed out that the inlet condition at different critical region play an important role to compressor efficiency and pressure ratio. These findings suggested strong influence of real gas properties on loss generation in the compressor. However, the mechanism of loss generation under the real gas properties effect has not been thoroughly explored.

Scholars have conducted studies on the design methodology of SCO_2 compressors, with a particular focus on predicting performance using a meanline model [13–20]. In general, the meanline model of a SCO_2 compressor is established based on the model using conventional fluids. For such a model, the coefficients of the loss models developed for conventional fluids are modified and calibrated for SCO_2. However, as there is no information on specific breakdown of the losses so far, it is difficult to further check the validity of various loss models for non-conventional fluids. In order to further optimize the model performance of the SCO_2 compressor under varying conditions, reliable loss models must be established based on sound understanding of the loss mechanism of the SCO_2 compressor.

Limited researches have been conducted to investigate the detailed loss mechanism of SCO_2 compressors. Seong's modified meanline model [13] found that main

loss sources within a compressor is contributed by wake loss, followed by tip clearance and incidence losses, with wall friction loss only making up a minor 2% contribution. Ameli et al. further explored the contribution of individual enthalpy losses in a SCO_2 compressor by using a one-dimensional loss model combined with NIST Refprop database [15]. The results indicated that the friction loss is a critical factor to internal loss sources, making up more than 25% of the overall losses - substantially larger than the 5–8% effect in air compressors [21, 22]. Furthermore, the major contributor to the losses is the incidence loss, forming about 30% of total value. According to these discussions, it can be inferred that the real gas properties have a noticeable influence on loss generation in the compressor. More importantly, the loss analysis described in the literature is all based on modified models designed for conventional fluids. However, there are no detailed discussions or validation of these loss models yet. And the modification based on the combination of traditional loss model could not reflect the difference between real gas properties of SCO_2 and air directly.

The present study aims to analyze the loss generation and corresponding flow mechanisms of a SCO_2 centrifugal compressor using three-dimensional numerical simulations. The cases using ideal CO_2 and ideal air were compared to illustrate the influence of real gas properties. The paper is comprised of three sections. Firstly, the numerical methods are described and validated against the experimental results. Next, the loss distribution in the impeller and diffuser is discussed and compared. Finally, the detailed flows corresponding to the loss generation are investigated.

2. Numerical Simulation Method

To validate the numerical simulation method, a Sandia SCO_2 centrifugal compressor was selected due to the availability of its experimentally obtained performance data in the literature [23]. As depicted in Fig. 1(a), the geometry of the compressor with vaned diffuser and volute were reconstructed based on the data in the literature [6, 23, 24]. The inlet temperature and pressure range for the test was 304.3 K to 307 K and 7700 kPa to 8139 kPa respectively, which was proximal to the supercritical point. The test was further validated at 50 000 rotations per minute.

The computational domains of the Sandia compressor are shown in Fig. 1(b) and (c). Structured meshes were applied for the impeller and diffuser using Autogrid module, while unstructured meshes were employed for the volute using Hexpress module. Autogrid is a module within the NUMECA software designed specifically for grid topological structuring and the generation of

high-precision structured grids for turbomachinery. Conversely, Hexpress is a module utilized for creating non-conformal, hexahedral unstructured grids on complex, arbitrary geometric shapes. These two modules are meshing modules that come with the Numeca Fineopen solver and offer high accuracy and quality. After conducting mesh independence analysis, there were 2.94 million nodes in a passage of the impeller and 0.8 million nodes in a passage of the diffuser. In addition, there were about 1.2 million nodes in the volute domain. Given that the Reynolds number of the SCO_2 compressor was about 2 orders higher than that of a conventional compressor, the grid size of the first layer was set to 10E–7 m, and the averaged y^+ of the calculation was less than 5 which was small enough to capture the features of the flow near the wall.

Table 1 Detailed geometric information of Sandia compressor

Components	Geometries	Values
Impeller	Blade height/mm	1.71
	Blade tip angle/(°)	–50
	Number of blade	6+6
	Radius of the impeller exit/mm	18.7
	Shroud radius/mm	9.37
	Hub inlet radius/mm	2.54
	Inlet blade angle at tip/(°)	50
	Tip clearance/mm	0.254
Vaned diffuser	Number of diffuser vanes	17
	Diffuser blade angle/(°)	68
Volute	Cross section ellipse ratio	1.1
	Outlet diameter/mm	32

The Reynolds-Averaged Navier-Stokes (RANS) equations were solved via Numeca, which is a density-based solver. The choice of turbulence model is very important for accurately capturing the details of internal flow of SCO_2 centrifugal compressor. Patel [25] compared the Boundary layer distribution calculated by DNS with various turbulence models, and showed that for SCO_2, Spalart-Allmaras (S-A) turbulence model can accurately reproduce the velocity and temperature profiles, with the smallest error compared with DNS data. What's more, the S-A model gave the most robust results compared with other models when solving turbulent flows with strong variation on the thermo-physical properties. And other authors also used this turbulence model for SCO_2/ORC turbomachinery after validation [26–29], which are also operating in the nonideal flow conditions. What's more, the influence of turbulence models on the Sandia SCO_2 centrifugal compressor is studied in the Appendix. The results showed that the S-A turbulence model had a minor error compared with other
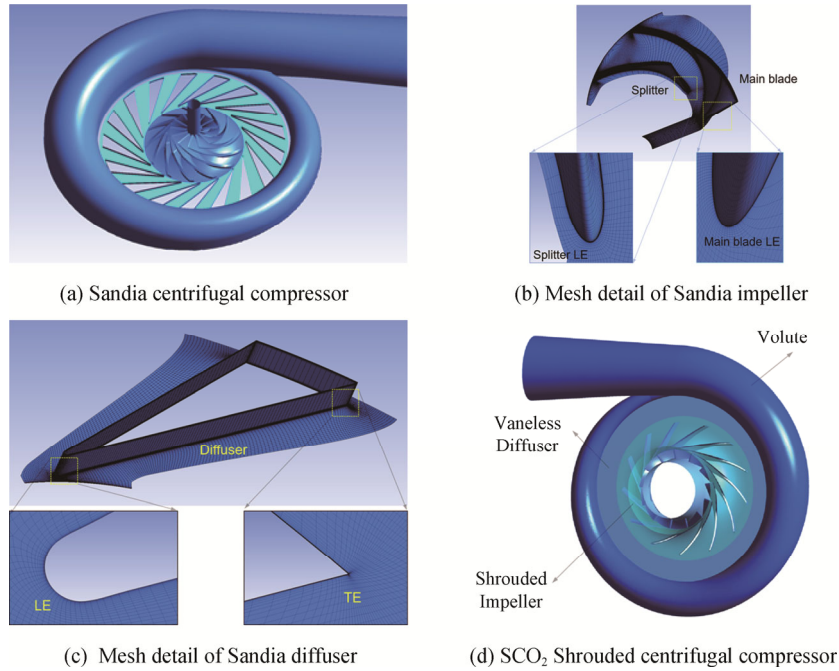
(a) Sandia centrifugal compressor

(b) Mesh detail of Sandia impeller

(c) Mesh detail of Sandia diffuser

(d) SCO_2 Shrouded centrifugal compressor

Fig. 1 SCO_2 centrifugal compressor model

the two models. Therefore, the S-A turbulence model was selected for the following numerical simulation. In addition, the central discretization scheme of second order accuracy was used for the artificial dissipation term. The conservative form of first order upwind was used for the convective terms to acquire convergence when large density gradients occur. And turbulence viscosity of 0.000 158 m^2/s was adapted in the inlet boundary condition which is calculated by the viscosity ratio of 10 recommended by the Numeca software for turbomachinery flow. The convergence criterion is set to 10^{-7} to determine whether the computation has converged, which corresponds to the order of the magnitude of the density, energy, and velocity residuals averaged over the computational domains. The fact that the residuals of the above terms meet the convergence criteria implies that the continuity, momentum and energy equations converge.

To ensure a reliable simulation of SCO_2, it is essential to present accurate modeling of real gas properties. The Span-Wagner equation of state (EOS) model is considered to be the most accurate one currently to calculate physical properties of CO_2 and has been embodied in the NIST Refprop standard reference database [30]. In our study, a table of real gas properties (RGP) based on Refprop was utilized. Three levels of precision were generated by the TabGen module for temperatures from 220 K to 600 K, and pressures from 4 MPa to 25 MPa: coarse (101×101), medium (301×301), and fine (401×401) precision. TabGen is a module that generates thermophysical property tables compatible with the NUMECA solver by inputting specific user parameters, such as the fluid's name and the equation of state used. It facilitates the creation of tables for different thermodynamic properties based on the provided user input. To verify the table independency, the influence of precision on predicted performance was checked. The results showed that the predicted efficiency and pressure ratio exhibited variations within 0.02% when the precision was Medium. Consequently, medium precision was chosen for the table in the study.

Total temperature (306 K) and total pressure (8 MPa) were applied as the inlet boundary conditions. Two outlet boundary conditions were set according to the operational conditions for the convergence. Specifically, the averaged static pressure was used under near-choke condition while the mass flow rate was used under near-surge condition. The walls boundary condition of compressor is considered to be adiabatic. A frozen rotor was applied for the interface between the impeller and the diffuser, and between the volute and the diffuser respectively in order to capture the interaction of the components to a certain degree. The rotation speed was fixed at 50 000 r/min according to the experimental condition.

For compressors, CFD calculations are prone to divergence when instability occurs under low flow conditions, especially when CO_2 exhibits significant physical changes near the critical point, which exacerbates the divergence under low flow rate conditions. Therefore, only high flow rate conditions are used for validation [6, 31]. Fig. 2 shows the predicted

results of the compressor, which are compared with the experimental results. The flow coefficient, efficiency and pressure ratio are respectively defined as follows:

$$\Phi = \frac{Q}{\rho_1 V_2 d_2^2} \tag{1}$$

$$\eta = \frac{h_{s2} - h_{s1}}{h_2 - h_1} \tag{2}$$
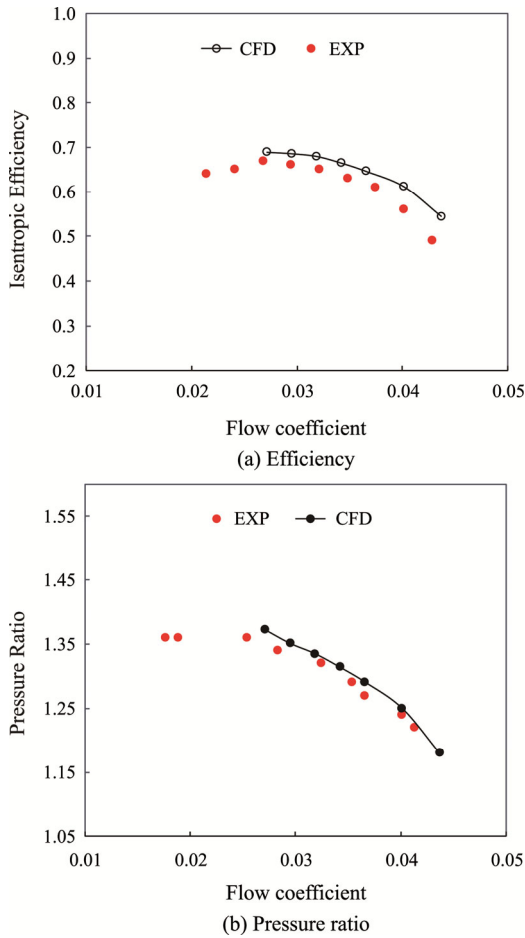
$$PR = \frac{P_{t,1}}{P_{t,2}} \tag{3}$$

(a) Efficiency

(b) Pressure ratio

Fig. 2 CFD (SCO₂) validation against the experiment

It was observed that the trend of predicted performance was in close agreement with the experimental results when compared with existing validations in published literature. Specifically, the predicted pressure ratio was just 1.5% greater than that in the experiment. The discrepancy of the efficiency between the two results was greater, but the averaged discrepancy was still within 4%. Several factors were considered to contribute to these discrepancies. First, as previously discussed, there were discrepancies in geometries between the simulation and the experiment

(especially for the volute). Second, the turbulence model which has been widely validated against conventional fluids was employed in the current simulation, but the uncertainty of the turbulence model concerning the real gas properties needs to be further validated with more sophisticated experimental or high-order CFD simulations. Nevertheless, validation of the CFD results suggested that the prediction was still satisfactory, giving rise to significant confidence in further researches.

3. Results Analysis

3.1 Influence of gas properties on loss distribution

Compared with the ideal air of conventional fluid, the density of SCO₂ is roughly 700 times larger. Furthermore, the properties of the SCO₂ fluid are highly contingent upon local pressure and temperature, and hence highly dependent on the flow field in the compressor. To study the influence of real gas properties on loss generation in the SCO₂ compressor, three fluids: SCO₂, ideal air (IAir) and ideal CO₂ (ICO₂), were used for direct comparison. The specific heat ratio for IAir was kept constant at 1.4, while that of ICO₂ was set to a constant value of 1.29 which was calculated from the relationship between universal gas constant and the molecular weight. Both of them satisfy the ideal air law. Thus, the differences between the results obtained for SCO₂ and ICO₂ were resulted from the interaction of flow field with properties in the compressor. Meanwhile, the differences between the results obtained for ICO₂ and IAir were resulted from the large discrepancies of fluid properties. The inlet condition for the case using ICO₂ was the same with that using SCO₂ at the compressor inlet, but the properties remained constant in the flow. In order to draw valid

Table 2 Boundary conditions of the three fluid cases

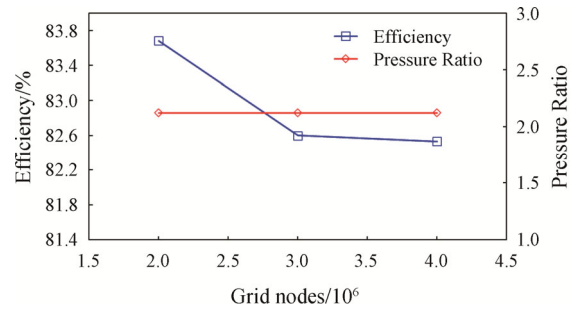|	Conditions	SCO₂	ICO₂	IAir
Inlet	Total pressure/MPa	8	8	0.1
	Total temperature/K	314	314	288
	Machine Mach number, M_{U2}	0.42	0.42	0.42

Fig. 3 Mesh independence analysis of SCO₂ Shrouded compressor

comparisons between different fluid cases, the Machine Mach number M_{U2} was kept the same to preserve dynamic similarity [9]. The resulted inlet boundary conditions of the three cases are shown Table 1. The method of comparison serves to illustrate the influence of real gas properties on the compressor performance and flow field.

To investigate the influence of fluid properties, a specifically designed SCO_2 centrifugal compressor for waste heat recovery in industrial vehicle was employed. The configuration of the compressor is shown in Fig. 1(d). This shrouded centrifugal compressor had 13 blades, a vaneless diffuser, and an overhang volute, with a design rotation speed of 60 000 r/min. The inlet conditions of the compressor are 314 K and 8 MPa, which are determined by the requirement of the cycle system. Firstly, the mesh independence analysis was carried out using SCO_2. As shown in Fig. 3, the pressure ratios obtained from the three kinds of grid are basically the same, while the efficiency obtained from the grid with 2 million nodes is greater than the other two, and the efficiency does not change significantly after the grid is larger than three million. Considering the calculation efficiency and accuracy, the number of grids is chosen to be 3 million for the subsequent numerical calculation and analysis.

The same numerical method validated previously on the Sandia SCO_2 compressor, including the setting of outlet and wall boundary conditions, was applied for the performance and flow simulation. Fig. 4 compares the efficiency and pressure ratio of the cases with three types of properties. There were notable differences between the cases using SCO_2 and ICO_2. The choke flow rate coefficient of SCO_2 was about 6% lower than that of ICO_2, resulting in lower pressure ratio and efficiency at low flow coefficient respectively, by roughly 5% and 3%. It can be inferred that the real gas properties had a significant influence on the flow in the compressor. When the mass flow rate was relatively low, the discrepancies of fluid properties with the flow field promoted the performance; however, this caused the compressor to experience early chokes. As shown in the figure, the case using IAir exhibited the most desirable performance among the three cases. Interestingly, the compressor performance of the case using IAir was similar to that using SCO_2 at low flow coefficients and to that using ICO_2 at high flow coefficients with discrepancies of less than 1.5%. The results of the comparison proved to be counterintuitive, as the properties of SCO_2 at high pressure tended to be closer to those of ICO_2 rather than IAir at the atmospheric pressure. The reasons for these behaviors will be further discussed in the following sections. Notably, the comparison results also validate that ideal air is appropriate in predicting the

performance of SCO_2 compressors at low mass flow rates when the operating condition is in the supercritical region away from the critical point. The differences of compressor performance between the ideal air and SCO_2 are expected to be larger than what observed in the current research when the operational point is closer to critical point, as the flow properties are much more sensitive to the temperature/pressure at the vicinity of critical point. But the differences between the SCO_2 and Ideal CO_2 are expected to be even larger, and thus the trend is similar as Fig. 4.
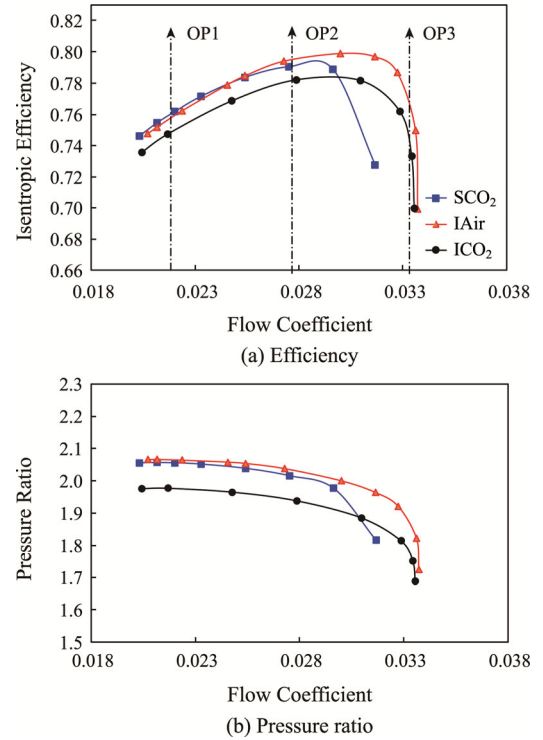

Fig. 4 Performance comparison of the cases with three types of properties

In order to find the main reasons for the performance discrepancies, the loss distribution of the compressor with three operating points, denoted in Fig. 4 as OP1, OP2, and OP3, were discussed. From the figure, OP2 represents the most efficient operating point for SCO_2, while OP1 and OP3 represent situations of low flow coefficient condition and near-choke condition, respectively. Specifically, the loss coefficient (entropy rise coefficient) is defined according to Eq. (4) [32], which is a metric to parameterize the contribution to overall efficiency decline.

$$\sigma = \frac{T_{1t}\Delta S}{h_{2t} - h_{1t}} \tag{4}$$

where, ΔS is the entropy rise of a component, which include the influence of fluid properties on the loss. T_{1t} is

the inlet total temperature; h_{2t} and h_{1t} are the total enthalpy at the exit and inlet of the compressor, respectively. The multiply of inlet temperature is a method to evaluate the loss of the flow availability due to the entropy generation in the fluid component. It can also be considered that inlet temperature is used to nondimensionalize the entropy generation.

Fig. 5 illustrates the breakdown of losses in the impeller and the volute (with the vaneless diffuser) for each of the three fluids at different conditions. At low flow coefficient and design conditions, the loss generated in the stator (volute and diffuser) was notably larger than that in the rotor for all the three fluids, but tended to equalize near choke condition except the impeller for SCO$_2$. The loss coefficient of the impeller for SCO$_2$ was the highest among the three fluids at all operational conditions, increasing by roughly 3 times to 0.12 for SCO$_2$ at OP3. However, the loss generated in the stator was the lowest for SCO$_2$, while the highest for ICO$_2$.

The discrepancies in loss distribution of the components were direct reasons for the performance as illustrated in Fig. 4. IAir achieved the highest efficiency in general, while ICO$_2$ yielded the lowest one, except for OP3. As the flow coefficient and machine Mach number were the same for the three fluids, the discrepancies in loss distribution can be attributed to the differences in the influence of fluid properties on the flow field. Furthermore, the differences in loss distribution in the stator were also resulted from the flow field in the impeller. Detailed comparisons on the flow field in the impeller are discussed in following sections.

3.2 Influence of flow properties on flow field

In order to understand the loss discrepancies in the compressor, a detailed flow field analysis among the three fluids was conducted. Despite the identical flow coefficient and machine Mach number, the entropy and enthalpy of the three fluids varied, and the coefficient of entropy rise was again used for the analysis of loss

generation distribution in the compressor. In particular, the distribution of entropy rise coefficient in Eq. (4) was relative to the value at the compressor inlet.

Fig. 6 illustrates the averaged entropy rise coefficient at 8 cross sections along the impeller passage for the three fluids at OP1 and OP3. The coefficient increased consistently along the passage for all the three fluids at OP1, indicating an accumulation of entropy as the flow went downstream in the rotor passage, as shown in Fig. 6(a). Notably, the entropy coefficient was the highest for SCO$_2$, followed by ICO$_2$, and the lowest for IAir. To pinpoint the regions with the highest entropy generation, local entropy generation accumulation was further illustrated in Fig. 6(b). Specifically, this was achieved by calculating the difference of the averaged coefficients between two consecutive sections of the flow. The results showed that for SCO$_2$, the highest entropy was generated in the range of about 10%–50% of the streamwise length; however, as the fluid changed from ICO$_2$ to IAir, this range gradually shifted to 20%–65%. Moreover, the maximum difference of entropy generation among the three fluids was observed within the first 50% of the streamwise length. Thus, it can be inferred that the influence of fluid properties was weighted heavily towards the front section of the impeller passage at OP1.

Fig. 6(c) and Fig. 6(d) further illustrate the entropy rise coefficient at OP3. The difference among various fluids was evidently larger at OP3 than that at OP1. The entropy rise coefficient of SCO$_2$ rised sharply in the streamwise direction, resulting in nearly two times of the value of IAir at the impeller exit. Furthermore, the coefficient of SCO$_2$ increased significantly from 18% of the streamwise length, which was surprisingly about 3 times the value for IAir and ICO$_2$. The high entropy generation of SCO$_2$ kept happening till about 90% of the streamwise length. This indicated that some flow structures with high entropy generation appeared in the region spanning 15% to 90%. The flow mechanism for this phenomenon will be discussed in more details in later sections.
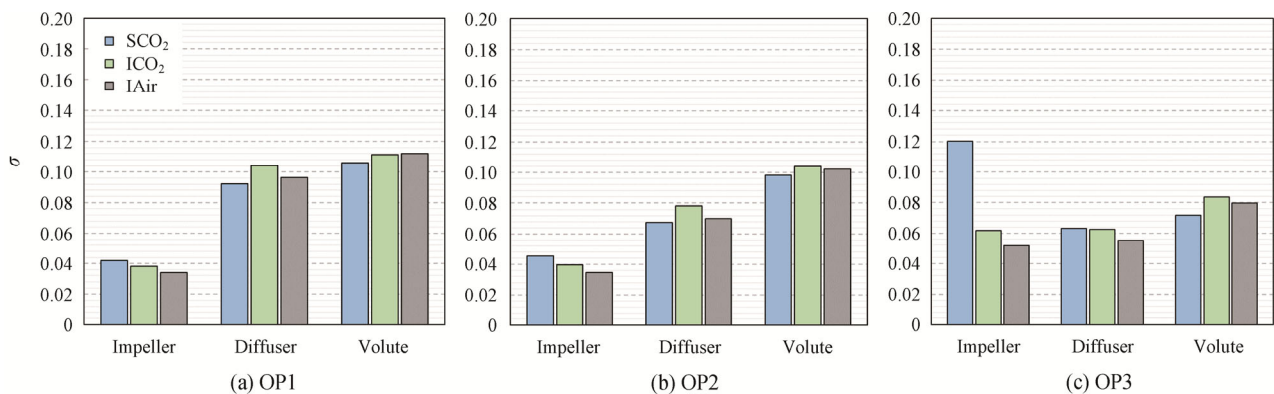

Fig. 5 Entropy coefficient of components using different fluids

(a) Entropy generation at OP1

(b) Entropy accumulation at OP1

(c) Entropy generation at OP3
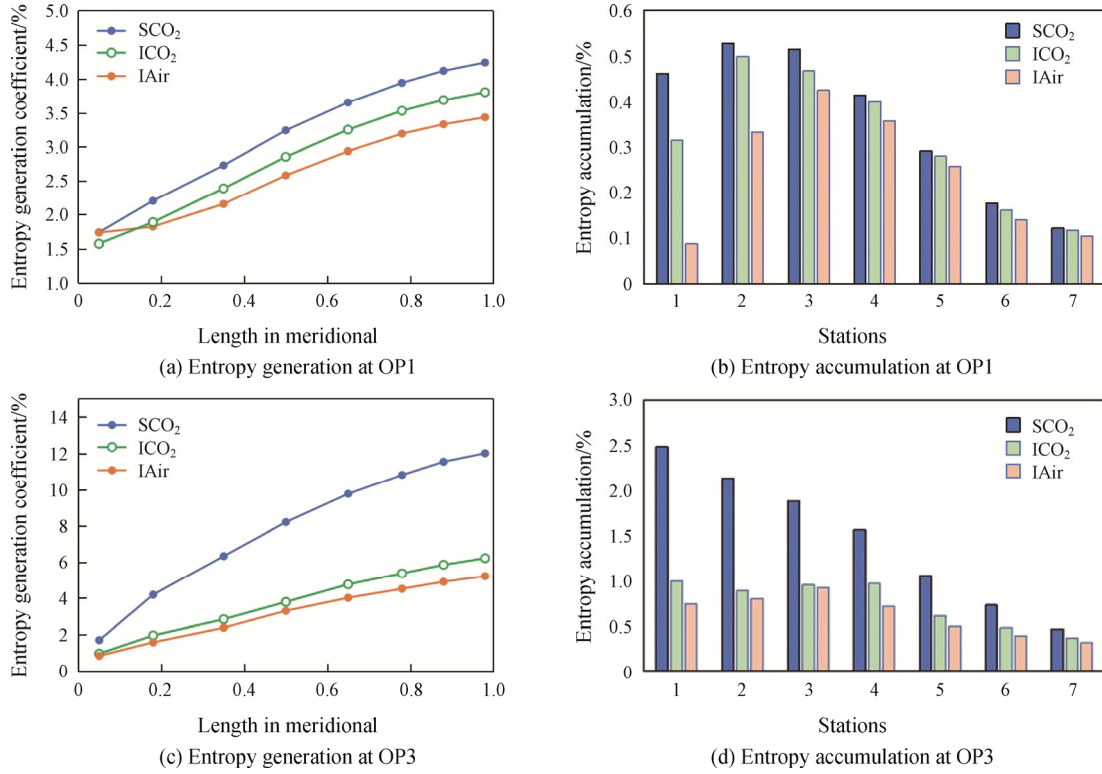
(d) Entropy accumulation at OP3

Fig. 6 Entropy rise coefficient along the impeller

The entropy was generated by two aspects for the investigated compressor with the assumption that the internal heat source can be neglected, as shown in Eq. (5). The index i here means that the temperature gradient is calculated in all directions (x, y, z). The equation is derived with the assumption that the internal heat source can be neglected. The first term on the right side of the equation is the dissipation due to flow viscosity and strain. The second one is the internal heat transfer arising from temperature gradients. To gain a better insight into the reasons for entropy generation, contribution of the two factors needs to be separately compared. The entropy generation equation was integrated to nine local volumes along the streamwise directions of the impeller passage, hence enabling the entropy generation to be conveniently tracked along the impeller passage. It is worth mentioning that the integrated entropy was finally dimensionless by Eq. (4) for the comparison of entropy generation among different fluids.

$$\rho \frac{\mathrm{d}S}{\mathrm{d}t} = \frac{\Phi}{T} + \frac{k}{T^2}\left(\frac{\partial T}{\partial x_i}\right)^2 \tag{5}$$

Fig. 7 compares the entropy generation resulted from viscosity dissipation and internal heat transfer, respectively, in consecutive volumes along the impeller passage for the three fluids at OP1. By comparison between the two subfigures, it was clearly seen that viscosity dissipation dominated the entropy generation
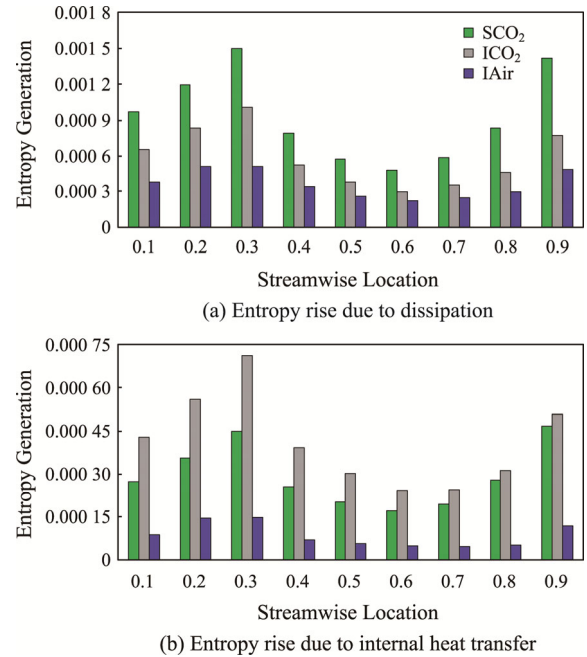

(a) Entropy rise due to dissipation

(b) Entropy rise due to internal heat transfer

Fig. 7 Entropy generation due to flow viscosity and internal heat transfer at OP1

for all the three fluids, with roughly two times higher than that of internal heat transfer. However, evident discrepancies can be observed among the three fluids. Particularly, when compared with ICO_2, SCO_2 has a

higher entropy generation due to dissipation but a notably lower value due to heat transfer. It is noteworthy that the viscosity and heat capacity of ICO_2 were identical to those of SCO_2 at the impeller inlet due to identical inlet conditions. Consequently, it can be inferred that the higher dissipation in SCO_2 was caused by intense straining or even stronger turbulence-induced viscosity in the impeller. Simultaneously, the lower internal heat transfer in the impeller was likely due to unignorable increase in heat capacity, which reduced the temperature gradient. The lowest entropy resulted from dissipation and heat transfer can be observed in the case using IAir, partially due to the comparatively low Reynolds number of the fluid.

Fig. 8 compares the distribution of entropy generation of the three fluids over two aspects at OP3. It was observed that the distribution followed a similar trend to that obtained at OP1. The dissipation dominated the entropy generation in the impeller. The entropy of dissipation for SCO_2 was larger than that of ICO_2, while the entropy of internal heat transfer was relatively lower. However, compared with OP1, substantial discrepancies in dissipation were observed among the three fluids at OP3, indicating larger differences of flow structures for the former operational condition.
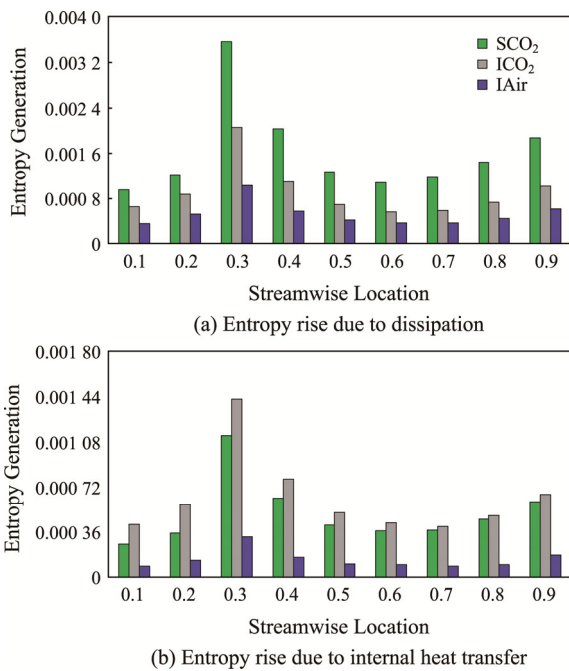

(a) Entropy rise due to dissipation

(b) Entropy rise due to internal heat transfer

Fig. 8   Entropy generation due to flow viscosity and internal heat transfer at OP3

Examining the distributions at the two operational conditions revealed that the majority of entropy rise occurred near the leading edge (0%–40% streamwise) and trailing edge (80%–90% streamwise) of the passage.

To further illustrate the associated flow structure, the distribution of entropy rise coefficient throughout the impeller was compared among the three fluids. In particular, the entropy generation was integrated into local volumes placed within a 10×10 matrix of streamwise and spanwise directions of the impeller passage, as shown in Fig. 9(a).

Fig. 9(b)–(d) illustrate the distribution of entropy rise coefficient of the three fluids in the impeller passage at OP1. It was observed that the pattern of the distribution was similar for SCO_2 and ICO_2, although the value of the former was slightly higher. In the region near the impeller end-wall, the differences in entropy rise coefficient are comparatively pronounced in the value, while the mainstream region remains essentially consistent. Therefore, it is reasonably inferred that the differences between SCO_2 and ICO_2 under near-surge conditions may be attributed to different behaviors of the gas property gradients near the wall. For real gases, the property gradients near the wall are more significant. In this study, for instance, the density gradient of SCO_2 near the wall reaches the order of 10E+6, whereas for the CO_2 ideal gas, it is only on the order of 10E+5. Meanwhile, compared with the former two fluids, IAir exhibited a lower degree of entropy increase. This result was consistent with the findings from Figs. 7 and 8. Examination of the contours revealed that higher entropy was generated in the five regions, labeled as A–E in the subfigures. Specifically, regions A and B locate at the shroud/hub near the leading edge respectively; region C aligns with the leading edge, and regions D and E locate at the shroud/hub near the trailing edge respectively. Such an observation clearly reflected that the discrepancies in entropy generation among the three fluids were induced by the flow structures near the end walls of the leading and trailing edges.

Since the differences of entropy rise coefficient distribution and flow structure in the impeller between SCO_2 and ICO_2 are not as obvious as that of IAir, the following section mainly concentrates on an in-depth discussion of the phenomenon that produces such a great difference between SCO_2 and IAir. Fig. 10(a) and (b) further compares the detailed distribution of entropy rise coefficient in the impeller passage corresponding to the regions with high entropy generation for SCO_2 and IAir. It should be mentioned that the used impeller was a closed one and thus experienced no tip clearance flow. Downstream the impeller's leading edge, the regions of high entropy generation were primarily near the shroud, hub and suction surface, which could be attributed to turbulent boundary layers on the walls. Moreover, under the complex couple effect of the multiple forces in the centrifugal impeller, such as centrifugal force and pressure gradient, the boundary layer accumulation was
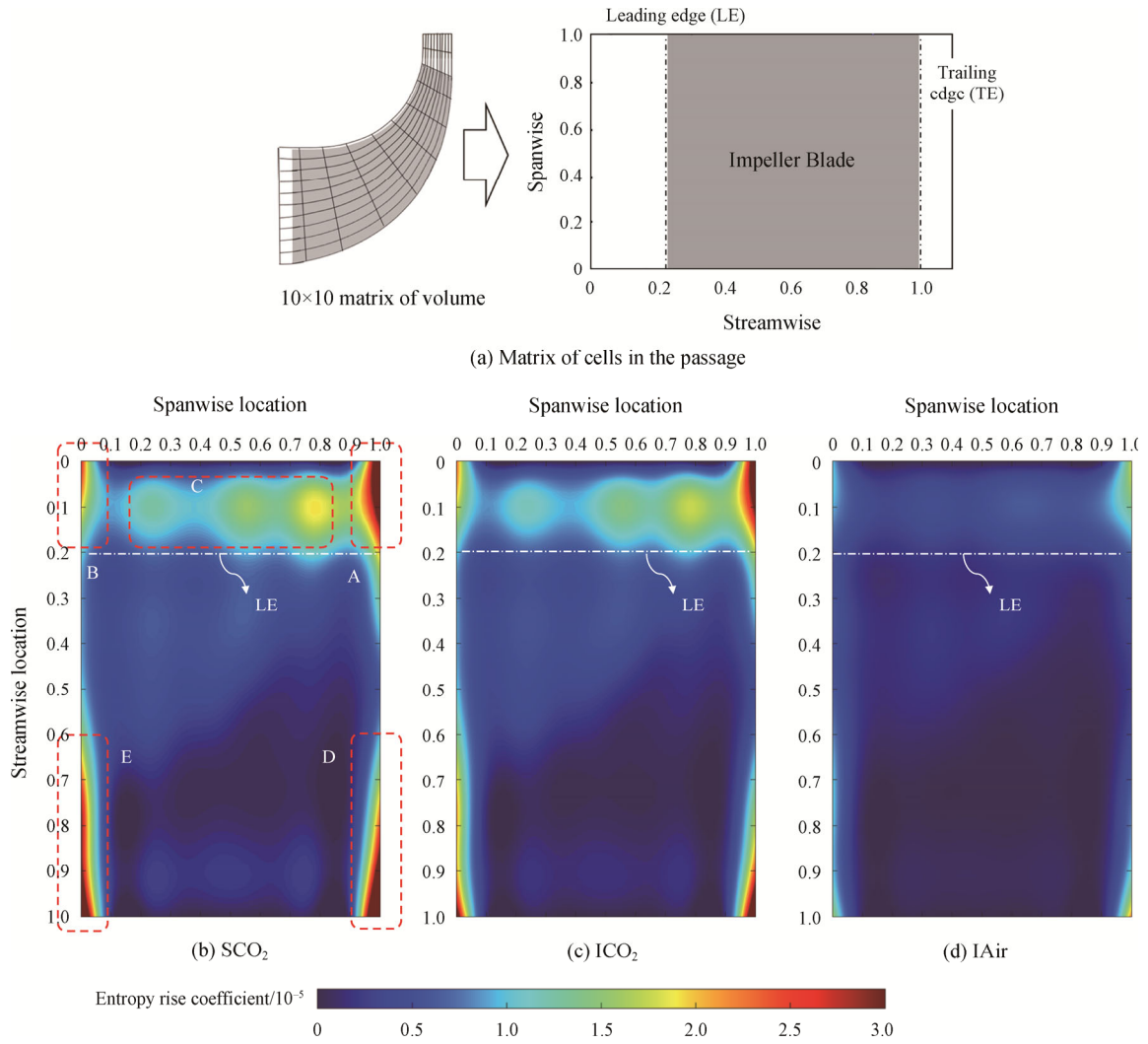
(a) Matrix of cells in the passage

(b) SCO₂   (c) ICO₂   (d) IAir

Fig. 9   Entropy rise for the three fluids at OP1

driven near the shroud region, leading to a notable rise in entropy generation near the suction surface on the shroud. When comparing entropy generation near the walls between SCO_2 and IAir, it was evident that higher entropy was generated by the former, hinting at a thicker boundary layer area and a lighter shade. Furthermore, as evident from the comparison of the relative Mach number distribution of two impellers in Fig. 10(c), a thicker boundary layer accelerates the separation of the boundary layer on the suction side of SCO_2 impeller. This implied that the boundary layer behavior varied significantly among different fluids.

The detailed force analysis in the centrifugal impeller was conducted to figure out the origin of the different boundary layer behavior. In a rotating impeller passage, dynamic balance was achieved by pressure gradient and Coriolis force in blade-to-blade direction, which means that the pressure gradient is indirectly proportional to the fluid density through the Coriolis force, and by pressure

gradient and centrifugal force in radial direction. But the Coriolis force and centrifugal force were both altered due to the reduced relative flow velocity found in the boundary layer. As a result, the development of the boundary layer was influenced by the imbalance of the two forces, as illustrated in Fig. 10(d). On the shroud and hub surface, the Coriolis force reduced notably due to relative low flow velocity in the boundary layer, permitting the pressure gradient of the main flow to penetrate the boundary layer. As a result, the boundary layers on these two surfaces were deflected towards the shroud of the suction surface. Noteworthily, since CO_2 is significantly denser than air in the supercritical region, the pressure gradient of SCO_2 and ICO_2 was roughly two orders higher than that of IAir, leading to a distinctly increased accumulation of the boundary layer on the suction surface (as shown in Fig. 10). Additionally, the greater density of SCO_2 and ICO_2 contributed to an even more substantial accumulation of boundary layers in the
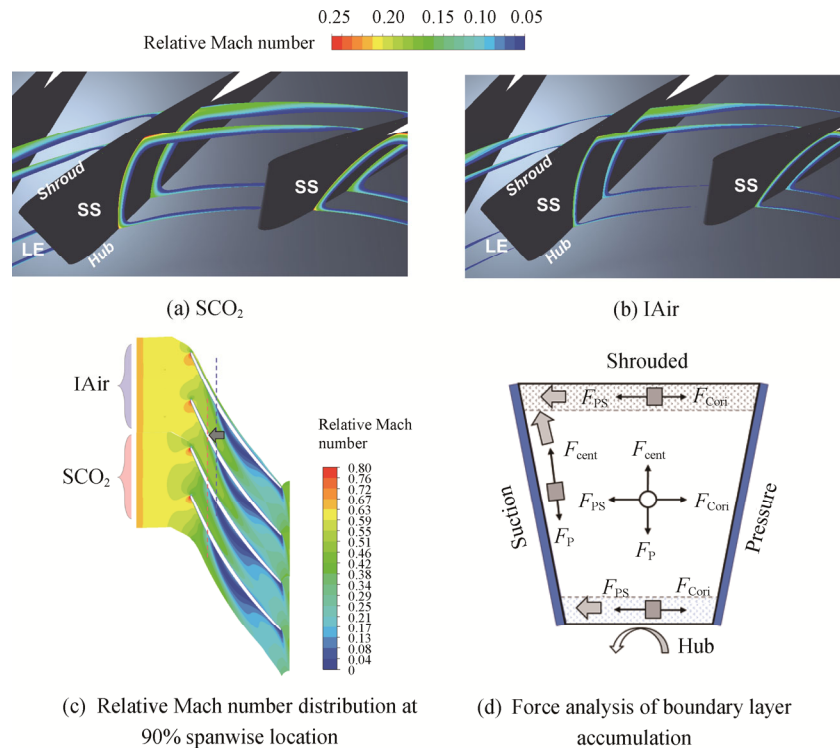
(a) SCO_2

(b) IAir

(c) Relative Mach number distribution at 90% spanwise location

(d) Force analysis of boundary layer accumulation

Fig. 10　Flow mechanism corresponding to high entropy generation

impeller passage. As mentioned above, the differences between SCO_2 and ICO_2 are primarily evident in the region near the wall, where the property gradient of SCO_2 is significantly stronger than that of ICO_2. A stronger property gradient will affect the turbulence activity within the boundary layer, potentially resulting in a stronger shear layer [33]. Therefore, the entropy rise in the boundary layer for ICO_2 is expected to be smaller compared to SCO_2, which aligns with the observations in Fig. 9.

A similar accumulation of low momentum flow was observed near the trailing edge of the impeller. Fig. 11 compares the contours of entropy rise coefficient at a section near the trailing edge for the three fluids at OP1. It can be seen that the region with high entropy appeared on the suction surfaces on this section for all the three fluids. This is a typical jet-wake pattern at the exit of a centrifugal impeller. The wake was resulted from the accumulation of low momentum flow in the passage, which was driven by both Coriolis force and centrifugal force. Similar as the mechanism near the leading edge, the low momentum flow for SCO_2 and ICO_2, caused by small Coriolis force, was strongly pushed towards the suction surface due to the pressure gradient being two orders higher than that of IAir. Consequently, the entropy rise was notably lower for IAir. Moreover, the subtle discrepancies of the patterns between SCO_2 and ICO_2 were resulted from the real gas properties of CO_2.
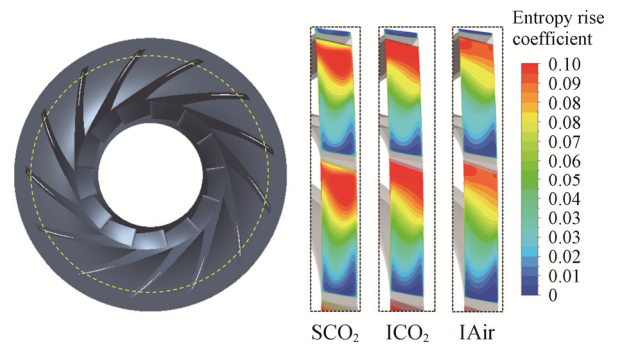

Fig. 11　Contours of entropy rise coefficient at the trailing edge of the impeller at OP1

Upon further examination of the jet-wake patterns at the exit of the impeller, it was observed that there were differences among the three fluids. For all the fluids, the region with high entropy generation was accumulated on the suction surface, but for SCO_2 it was mostly concentrated around the mid-height of the blade; for both ICO_2 and IAir, it appeared near the hub surface. It indicated that the migration and accumulation of secondary flow in the centrifugal impeller was influenced by the real gas properties of SCO_2. This discrepancy of jet-wake pattern inevitably influences the blockage and flow condition of the vaneless diffuser downstream the impeller. The dimensionless velocity V_n at the exit of the impeller for SCO_2 is about 8% lower than that of IAir,
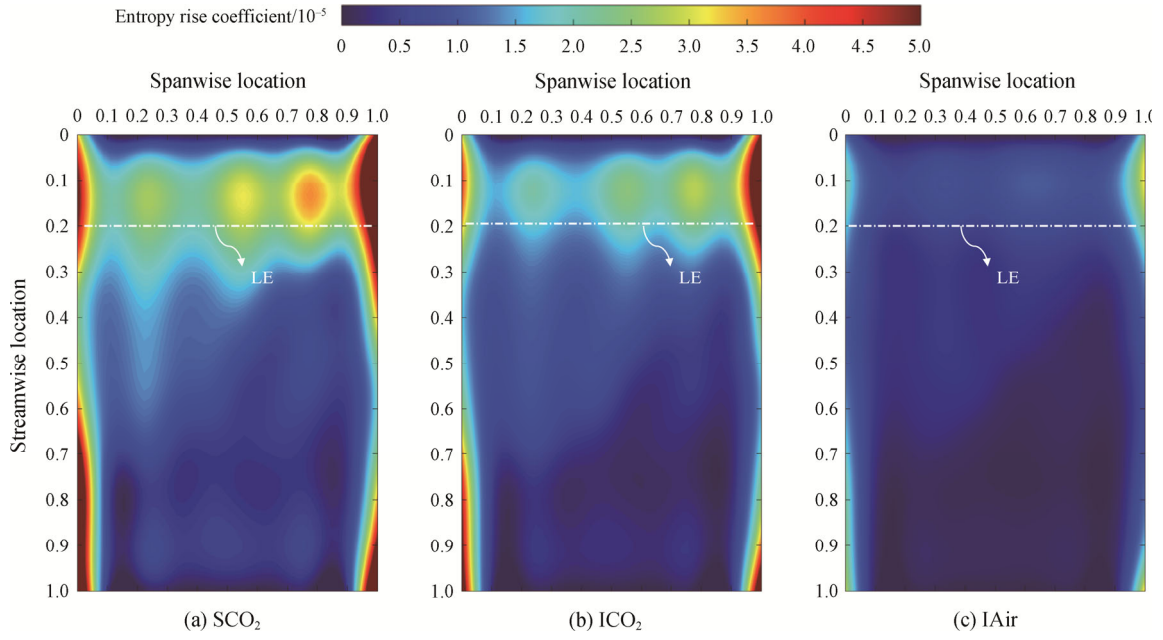
Fig. 12 Entropy rise for the three fluids at OP3

which is defined as the ratio of the local mass-flow-rate averaged velocity to the impeller blade tip velocity at trailing edge. Furthermore, the skin friction coefficient of a vaneless diffuser is inversely proportional to the Reynolds number to the power of 0.2, as shown in Eq. (7) [34]. Therefore, the skin friction loss of SCO_2 in the diffuser and volute is notably lower than that of IAir. Due to the combined influence of flow pattern at the inlet, velocity and friction coefficient, the entropy rise of the three fluids was found to be distributed as demonstrated in Fig. 9.

$$V_n = \frac{V_{ave}}{V_2} \qquad (6)$$

$$C_f = k\left(\frac{1.8 \times 10^5}{Re}\right)^{0.2} \qquad (7)$$

Fig. 12 shows the entropy coefficient for the three fluids under high flow coefficient condition at OP3. The distribution patterns were similar as the condition of OP1. The entropy generated was the highest in the case using SCO_2, followed by ICO_2 and then IAir. There were five distinct, high-entropy-generating regions in the passage. However, in comparison to OP1, the discrepancies between SCO_2 and ICO_2 were noticeably increased. Especially, both the size and intensity of region C directly downstream of the leading edge were far more prominent for SCO_2. This indicated that the real gas properties of SCO_2 significantly increased the flow structures resulting in a high entropy.

As OP3 was close to the choke condition, the entropy generation was augmented owing to the shockwave-induced losses caused by the disparities of
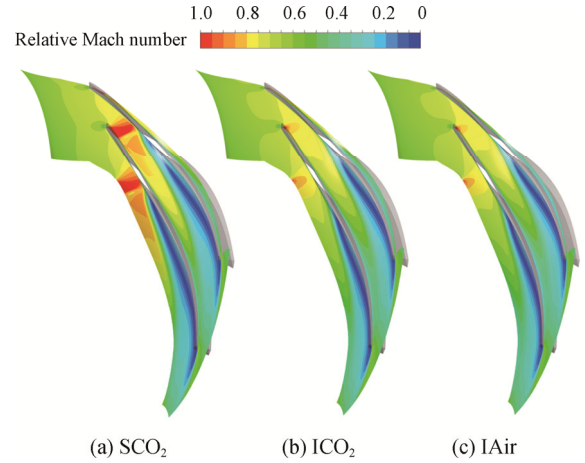

Fig. 13 Relative Mach number at 80% blade height at OP3

sonic speeds among the three fluids. Fig. 13 illustrates the distribution of relative Mach number at 80% blade height for the three fluids at OP3. Notably, a stark shockwave was visible at the throat of the passageway located 25% downstream the leading edge for SCO_2. Furthermore, the shockwave impinged on the suction surface of the adjacent blade, resulting in a rapid separation of the boundary layer due to the presence of a strong adverse pressure gradient. For ICO_2 and IAir, the shockwave was not visible, and the boundary layer separation was considerably delayed and less pronounced after the throat. On the other hand, the phenomenon of shock wave-induced boundary layer separation also explains the significantly larger dissipation produced by SCO_2 than the other two fluids in Fig. 8(a) at the 0.3–0.4 streamwise locations (about 25% downstream from LE).

It can be inferred that the choke of the passage had already occurred for SCO$_2$, but not yet for ICO$_2$ and IAir. This was the reason for the higher entropy in the fluid of SCO$_2$ as discussed in Fig. 6(c)–(d).

4. Conclusions

SCO$_2$ centrifugal compressor is a key component of a closed Brayton cycle, providing a notable advantage in terms of higher efficiency and higher power density. Performance predictions obtained by the meanline model are mostly achieved through conventional fluid methodologies. This paper presents a comparative analysis on aerodynamic losses in a SCO$_2$ centrifugal compressor, yielding the following four main conclusions in the case that SCO$_2$ compressor working at supercritical state away from the critical point:

(1) While maintaining the dynamic similarity at the same machine Mach number, the pressure ratio and efficiency of the SCO$_2$ centrifugal compressor were similar to those of IAir compressors at low flow coefficient conditions, but significantly lower than those of both IAir and ICO$_2$ compressors as the flow approached choke conditions. Moreover, the choke flow rate boundary of the SCO$_2$ compressor was 6% smaller than that of IAir and ICO$_2$ compressors. It is noteworthy that this conclusion is derived from 3D CFD analysis involving three distinct fluids, contrasting with Baltadjiev's approach [9] of utilizing 2D CFD analysis to examine various inlet conditions of SCO$_2$.

(2) A comparison of the loss distribution of the compressors revealed that the losses in the impeller were the highest for SCO$_2$, followed by ICO$_2$ and IAir. As the flow coefficient increased, the discrepancies in loss distribution were significantly enlarged. In contrast, SCO$_2$ exhibited the lowest losses in the stator, including the diffuser and volute.

(3) The discrepancies of loss generation among the three fluids were mainly observed in the regions up to about 50% of the streamwise length in the impeller passage. Entropy generation was the highest in five regions on the shroud/hub surface near the leading and trailing edges, for both low and high flow coefficients.

(4) The high entropy generation on the shroud surface was caused by an imbalance in forces, namely the difference between the blade-to-blade pressure gradient and Coriolis force in the boundary layer, and between the centrifugal force and hub-to-shroud pressure gradient on suction surface. Moreover, due to the larger pressure gradients for SCO$_2$ and ICO$_2$, the boundary layer accumulation of these two fluids was noticeably larger than that of IAir, consequently generating higher entropies in their vicinity.

(5) Compared to the impeller working with IAir and ICO$_2$, that with SCO$_2$ was choked at an earlier stage due to its smaller sonic speed. As a result, the entropy generation induced by the shockwave near the throat for SCO$_2$ was notably greater than the other two fluids.

Acknowledgement

Conflict of Interest

On behalf of all authors, the corresponding author states that there is no conflict of interest.

Electronic Supplementary Materials

Supplementary materials are available in the online version of this article at
https://doi.org/10.1007/s11630-024-2027-8

References

[1] Angelino G., Carbon dioxide condensation cycles for power production. Journal of Engineering for Power, 1968, 90(3): 287–295.

[2] Feher E.G., The supercritical thermodynamic power cycle. Energy conversion, 1968, 8(2): 85–90.

[3] Liu Y., Wang Y., Huang D., Supercritical CO$_2$ Brayton cycle: A state-of-the-art review. Energy, 2019, 189: 115900.

[4] Zhang R., Su W., Lin X., Zhou N., Zhao L., Thermodynamic analysis and parametric optimization of a novel S-CO$_2$ power cycle for the waste heat recovery of internal combustion engines. Energy, 2020, 209: 118484.

[5] Persichilli M., Kacludis A., Zdankiewicz E., Held T., Supercritical CO$_2$ power cycle developments and commercialization: why SCO$_2$ can displace steam. Power-Gen India & Central Asia, 2012.

[6] Pecnik R., Rinaldi E., Colonna P., Computational fluid dynamics of a radial compressor operating with supercritical CO$_2$. Journal of Engineering for Gas Turbines and Power, 2012, 134(12): 122301.

[7] Yang J., Yang Z., Duan Y., Design optimization and operating performance of S-CO$_2$ Brayton cycle under fluctuating ambient temperature and diverse power demand scenarios. Journal of Thermal Science, 2024, 33(1): 190–206.

[8] Yang Z., Jiang H., Zhuge W., Cai R., Yang M., Chen H., Zhang Y., Flow loss mechanism in a supercritical carbon dioxide centrifugal compressor at low flow rate

conditions. Journal of Thermal Science, 2024, 33(1): 114–125.

[9] Baltadjiev N.D., Lettieri C., Spakovszky Z.S., An investigation of real gas effects in supercritical CO_2 centrifugal compressors. Journal of Turbomachinery, 2015, 137(9): 091003.

[10] Kim S.G., Lee J., Ahn Y., Lee J.I., Addad Y., Ko B., CFD investigation of a centrifugal compressor derived from pump technology for supercritical carbon dioxide as a working fluid. The Journal of Supercritical Fluids, 2014, 86: 160–171.

[11] Saravi S., Tassou S., An investigation into sCO2 compressor performance prediction in the supercritical region for power systems. Energy Procedia, 2019, 161: 403–411.

[12] Karaefe R.E., Post P., Sembritzky M., Numerical investigation of a centrifugal compressor for supercritical CO_2 cycles. In: Proceedings of the ASME Turbo Expo 2020: Power for Land, Sea, and Air, online, 2020, September 21–25, Paper No: GT2020-15194, V011T31A011.

[13] Lee J., Lee J.I., Ahn Y., Yoon H., Design methodology of supercritical CO_2 Brayton cycle turbomachineries. In: Proceedings of the ASME Turbo Expo 2012: Turbine Technical Conference and Exposition, Copenhagen, Denmark, 2012, June 11–15, Paper No: GT2012-68933, pp. 975-983.

[14] Monje B., Sánchez D., Savill M., Pilidis P., Sánchez T., A design strategy for supercritical CO_2 compressors. In: Proceedings of the ASME Turbo Expo 2014: Turbine Technical Conference and Exposition, Düsseldorf, Germany, 2014, June 16–20, Paper No: GT2014-25151, V03BT36A003.

[15] Ameli A., Afzalifar A., Turunen-Saaresti T., Backman J., Centrifugal compressor design for near-critical point applications. Journal of Engineering for Gas Turbines and Power, 2019, 141(3): 031016.

[16] Cho S.K., Bae S.J., Jeong Y., Lee J., Lee J.I., Direction for high-performance supercritical CO_2 centrifugal compressor design for dry cooled supercritical CO_2 Brayton cycle. Applied Sciences, 2019, 9(19): 4057.

[17] Jeong Y., Son S., Cho S. K., Evaluation of supercritical CO_2 compressor off-design performance prediction methods. Energy, 2020, 213: 119071

[18] Cho, S.K., Son S., Lee J., Lee S.W., Jeong Y., Oh B.S., Lee J.I., Optimum loss models for performance prediction of supercritical CO_2 centrifugal compressor. Applied Thermal Engineering, 2021, 184: 116255.

[19] Xia W., Zhang Y., Yu H., Han Z., Dai Y., Aerodynamic design and multi-dimensional performance optimization of supercritical CO_2 centrifugal compressor. Energy Conversion and Management, 2021, 248: 114810.

[20] Xu P., Zou Z., Fu C., Aerodynamic design considerations for supercritical CO_2 centrifugal compressor with real-gas effects. Energy Conversion and Management, 2022, 271: 116318.

[21] Denton J.D., Loss mechanisms in turbomachines. Proceedings of the ASME 1993 International Gas Turbine and Aeroengine Congress and Exposition, Ohio, USA, 1993, May 24–27, Paper No: 93-GT-435, V002T14A001.

[22] Sundström E., Kerres B., Sanz S., Mihăescu M., On the assessment of centrifugal compressor performance parameters by theoretical and computational models. In: Proceedings of the ASME Turbo Expo 2017: Turbomachinery Technical Conference and Exposition, North Carolina, USA, 2017, June 26–30, Paper No: GT2017-65230, V02CT44A029.

[23] Wright S.A., Radel R.F., Vernon M.E., Rochau G.E., Pickard P.S., Operation and analysis of a supercritical CO_2 Brayton cycle. Sandia Report, No. SAND2010-0171, 2010.

[24] Rinaldi E., Pecnik R., Colonna P., Steady state CFD investigation of a radial compressor operating with supercritical CO_2. In: Proceedings of the ASME Turbo Expo 2013: Turbine Technical Conference and Exposition, San Antonio, Texas, USA, 2013, June 3–7, Paper No: GT2013-94580, V008T34A008.

[25] Patel A., Diez R., Pecnik R., Turbulence modelling for flows with strong variations in thermo-physical properties. International Journal of Heat and Fluid Flow, 2018, 73:114–123.

[26] Anand N., Vitale S., Pini M., Otero G.J., Pecnik R., Design methodology for supersonic radial vanes operating in nonideal flow conditions. Journal of Engineering for Gas Turbines and Power, 2019, 141(2): 022601.

[27] Rinaldi E., Pecnik R., Colonna P., Unsteady operation of a highly supersonic organic rankine cycle turbine. Journal of turbomachinery, 2016, 138(12): 121010.

[28] Wheeler A. P., Ong J., A study of the three-dimensional unsteady real gas flows within a transonic ORC turbine. In ASME Turbo Expo 2014: Turbine Technical Conference and Exposition, Wind Energy. Düsseldorf, Germany. June 16–20, 2014. Paper No: GT2014-25475, V03BT26A003.

[29] Shao W., Yang J., Wang X., Ma Z., Accuracy study and stability control of a property-table-based CFD strategy for modeling SCO2 compressors working near the critical point of the fluid. Applied Thermal Engineering, 2021, 183: 116222.

[30] Lemmon E., Huber M., McLinden M., NIST Standard Reference Database 23, NIST Reference Fluid Thermodynamic and Transport Properties Database (REFPROP): Version 9.1. National Institute of Standards

and Technology, 2007.

[31] Ameli A., Afzalifar A., Turunen-Saaresti T., Backman J., Effects of real gas model accuracy and operating conditions on supercritical CO_2 compressor performance and flow field. Journal of Engineering for Gas Turbines and Power, 2018, 140(6): 062603.

[32] Greitzer E.M., Tan C.S., Graf M.B., Internal flow concept

and applications, Cambridge University Press, 2004.

[33] Patel A., Boersma B.J., Pecnik R., The influence of near-wall density and viscosity gradients on turbulence in channel flows. Journal of Fluid Mechanics, 2016, 809: 793–820.

[34] Japikse D., Centrifugal compressor design and performance, 1996.